Original Research Article

International journal of spray and combustion dynamics

International Journal of Spray and Combustion Dynamics
2023, Vol. 15(4) 218–236

DOI: 10.1177/17568277231183047
journals.sagepub.com/home/scd

Sage

Uncertainty quantification analysis of Reynolds-averaged Navier–Stokes simulation of spray swirling jets undergoing vortex breakdown

Jacopo Liberatori[1], Riccardo M. Galassi[1], Mauro Valorani[1] and Pietro P. Ciottoli[1]

Abstract

The computational fluid dynamics-based design of next-generation aeronautical combustion chambers is challenging due to many geometrical and operational parameters to be optimized and several sources of uncertainty that arise from numerical modeling. The present work highlights the potential benefits of exploiting Bayesian uncertainty quantification at the preliminary design stage. A prototypical configuration of an acetone/air spray swirling jet is investigated through an Eulerian–Lagrangian method under non-reactive conditions. Two direct numerical simulations (DNSs) provide reference data, coping with different vortex breakdown states. Consequently, a set of Reynolds-averaged Navier–Stokes simulations is conducted. Polynomial chaos expansion (PCE) is adopted to propagate the uncertainty associated with the spray dispersion model and the turbulent Schmidt number, delivering confidence intervals and the sensitivity of the output variance to each uncertain input. Consequently, the most significant sources of modeling uncertainty may be identified and eventually removed via a calibration procedure, thus making it possible to carry out a combustion chamber optimization process that is no longer affected by numerical biases. The uncertainty quantification analysis in the current study demonstrates that the spray dispersion model slightly affects the fuel vapor spatial distribution under vortex breakdown flow conditions, compared with the output variance induced by the selection of the turbulent Schmidt number. As a result, additional high-fidelity experimental and numerical campaigns should exclusively address the development of an ad hoc model characterizing the spatial distribution of the latter in the presence of vortex breakdown phenomenology, discarding any effort to improve the spray dispersion formulation.

Keywords

Aerospace propulsion, computational fluid dynamics, uncertainty quantification, multiphase flows, vortex breakdown

Date received: 18 March 2023; accepted: 24 May 2023

Introduction

The aeronautics sector is currently at a crucial juncture, tasked with formulating innovative strategies to enable the creation of a climate-neutral aviation system by the mid-point of the century. To achieve this objective, it is imperative that the industry devise fresh approaches to aircraft system design, including the development of pioneering combustion devices, in order to adhere to new international benchmarks for aviation that prioritize safety, reliability, affordability, and environmental sustainability. In particular, the development of ultra-efficient thermal propulsion systems is critical for effectively transitioning to low- or zero-emission energy sources. The latter include synthetic fuels and non-drop-in fuels,[1,2] i.e., fuels that cannot be directly incorporated into existing airport infrastructures and aircraft fueling systems, such as hydrogen. Regarding the employment of hydrogen, the envisaged roadmap should overcome numerous challenges at the engine level.[3] Among these, we recall: (a)

[1]Sapienza, Università di Roma, Department of Mechanical and Aerospace Engineering, Rome, Italy

Corresponding author:
Jacopo Liberatori, Department of Mechanical and Aerospace Engineering, Sapienza, Università di Roma, Rome 00184, Italy.
Email: jacopo.liberatori@uniroma1.it

fuel system requirements,[4] including fuel temperature and vapor pressure control, heating from cryogenic to combustor temperature, improved sealing to prevent hydrogen leakage, and hydrogen embrittlement,[5] (b) operative challenges, such as altitude relight capability,[6] (c) combustor arrangement, including fuel injection and flow control, nitrogen oxides (NOx) control, flashback, and autoignition mitigation,[7] (iv) installation, primarily the integration of hydrogen storage on board.[8] Given these considerations, the final entry into service of next-generation low/zero-carbon ultra-efficient aircraft engines potentially involves a disruptive re-thinking of the entire combustion device, especially in the case of hydrogen-powered aviation.

In this sense, the full exploitation of computer-aided engineering coupled with design optimization methods represents a long-standing objective of the aviation sector, targeting the partial or complete replacement of vast, expensive, and practically difficult experimental campaigns. Therefore, the exploration of cost-effective but still reliable design optimization methodologies based on computational fluid dynamics (CFD) represents an unavoidable part of the renewal process of the aviation sector toward climate neutrality. However, while CFD modeling of turbulent reacting flows has been consolidated over the last decades,[9–11] its predictive capability correlates with the range of resolved fluid-dynamic scales. In this sense, direct numerical simulation (DNS) aims to resolve the instantaneous range of scales occurring in a turbulent flow, limiting its applicability to real industrial cases. Similarly, the large eddy simulation (LES) approach aims at resolving the spatially filtered values of the state vector while modeling the sub-grid variance, which still results in an unreasonable computational cost in the perspective of an ever-increasing amount of design challenges. Lastly, the low-fidelity level consists of Reynolds-averaged Navier–Stokes (RANS) modeling, which solves for the ensemble averages of kinematic and thermodynamic states and models their fluctuations while maintaining an affordable computational cost. However, the predictive accuracy associated with the RANS approach cannot be assessed a priori.

Furthermore, the characterization of an aeronautical combustion system needs to consider several interacting phenomena, e.g., liquid fuel injection, atomization, evaporation, gas-phase mixing, and chemical reactions, to name a few, resulting in a multi-physics, multi-scale, and multi-phase problem. In this regard, numerical simulations of diluted spray turbulent jets have been primarily performed in the last decades resorting to the Eulerian approach for the carrier fluid dynamics and the Lagrangian tracking of the dispersed phase,[12–17] equipped with a variety of spray sub-grid models. Although these sub-models are grounded on a physical foundation, they are characterized by several empirical parameters whose experimental calibration is either unfeasible or naturally uncertain, regardless of the level of numerical modeling adopted. In this sense, significant sources of uncertainty would eventually arise in DNS and LES approaches as well.

The uncertainty quantification (UQ) framework perfectly fits into this context and constitutes a helpful tool to identify, circumscribe and eventually reduce the uncertainties associated with model parameters. In particular, a Bayesian setting may be adopted to represent the degree of belief about the parameters of interest in terms of probability theory.[19] To this end, a strategy that hinges on both backward—or inverse—and forward UQ may be exploited to calibrate sub-model parameters and propagate their uncertainty to the quantities of interest (QoIs). More specifically, reference data provided experimentally or via DNS, if available, may be exploited to perform an inverse UQ analysis, which returns a representation of the uncertain parameters in terms of probability density functions (PDFs), that allow for a complete exploration of the input space.[20–23] Once the PDFs are known, the sub-model uncertainty may be propagated to the QoIs through low-fidelity RANS simulations, employing a polynomial chaos expansion (PCE) representation of the random variables (RVs) being involved to reduce the number of required simulations.[24–28] This way, CFD results become supported by reliability measures, such as error bars or confidence intervals, similar to the usually adopted representations of experimental results. Moreover, the derivation of a surrogate model in terms of a PCE naturally offers the opportunity to assess the sensitivity of the output variance to each uncertain parameter, e.g., in terms of the so-called Sobol indices. The embedded sensitivity analysis is crucial in identifying the major sources of computational model uncertainty so that the most influencing parameters may be properly calibrated before the design optimization process begins.

The present work is framed in a larger research project aimed at the numerical modeling of multiphase reacting flows in aeronautical and liquid rocket propulsion via RANS and LES approaches,[29,30] where the insights into the spray structure and gas-liquid interaction provided by DNS serve as a high-fidelity benchmark. In particular, it focuses on the critical issues arising during the numerical characterization of dry-low-emission (DLE) swirl-stabilized combustors. The DLE systems represent a long-standing technology in the aeronautics industry,[31–33] due to their capacity to provide a dominant flame stabilization mechanism. The latter is achieved through the onset of a central toroidal recirculation zone, induced by either a bubble-type or regular conical vortex breakdown (VB).[34,35] The aerodynamic flame stabilization overcomes the critical issue of combustion instability in lean premixed pre-vaporized (LPP) combustors,[39,40] as a result of being operated in the proximity of the lean blowout (LBO) limit.[41,42] A prototypical configuration of an acetone/air spray swirling jet exiting an abrupt expansion is

investigated here. The focus is on the forward propagation of the uncertainty associated with the computational model. This has to be intended as a preliminary feasibility study that paves the way for a thorough analysis of the combination of inverse and forward UQ frameworks to efficiently quantify and, eventually, reduce any source of uncertainty arising from numerical modeling in anticipation of CFD-based design optimization of a combustion device.

In the following, attention is given to two different sources of uncertainty, which are addressed according to separate approaches. In the first place, uncertainty is ascribed to the choice of the spray dispersion model. In this regard, following the work by Mueller and Raman,[43] a *peer* model approach is adopted; namely, a candidate model and a peer model are selected to reproduce liquid droplet dispersion in the RANS approach. Given that such models are physically plausible but still diverge one from another in terms of underlying physical assumptions, so as to ensure wide model variability, a stochastic spray dispersion model is formulated through a blending stochastic parameter ranging from zero to unity. Therefore, the uncertainty is concentrated into the blending coefficient, which is assigned an ad hoc probability distribution based on the plausibility of any combination of the peer models. On the other hand, the second source of uncertainty is ascribed to the selection of the turbulent Schmidt number, which regulates the estimation of the turbulent scalar fluxes. The forward uncertainty propagation is accomplished via two sets of RANS simulations, addressing both a low- and high-swirl regime. The results are compared with high-fidelity data provided by DNS calculations performed on the same test case configuration.

Numerical modeling

The Eulerian-Lagrangian numerical approach, the computational domain discretization, and the boundary conditions are described here below.

Eulerian-Lagrangian method

The following equations describe the turbulent Eulerian carrier phase in the DNS framework:

$$\frac{\partial \rho}{\partial t} + \frac{\partial (\rho u_j)}{\partial x_j} = S_m, \tag{1}$$

$$\frac{\partial (\rho u_i)}{\partial t} + \frac{\partial}{\partial x_j}\left[\rho u_i u_j + p\delta_{ij} - \tau_{ij}\right] = \rho g_i + S_{p,i}, \tag{2}$$

$$\frac{\partial \rho h_t}{\partial t} + \frac{\partial}{\partial x_j}\left[\rho h_t u_j + q_j\right] = \frac{\partial p}{\partial t} + \rho(u_i g_i) + S_e, \tag{3}$$

$$\frac{\partial \rho y_k}{\partial t} + \frac{\partial}{\partial x_j}\left[\rho y_k u_j + J_j\right] = S_{m,k}, \tag{4}$$

where ρ is the density, y is the mass fraction of the species k, J_i is the diffusive term, u_i is the velocity in direction i, p is the pressure, τ is the viscous stress tensor, h_t is the total enthalpy, given by the sum of sensible enthalpy and kinetic energy, q is the heat transfer rate, and g_i is the gravity acceleration in direction i.

The RHS terms are the coupling terms, consisting of the contribution of Lagrangian droplets in terms of mass, momentum, energy, and species concentration on the Eulerian gaseous medium. These are expressed as:

$$S_m = -\sum_{i=1} \frac{dm_{d,i}}{dt}\delta(x - x_{d,i}), \tag{5}$$

$$S_p = -\sum_{i=1} \frac{d(m_{d,i}u_{d,i})}{dt}\delta(x - x_{d,i}), \tag{6}$$

$$S_e = -\sum_{i=1} \frac{d(m_{d,i}c_l T_{d,i})}{dt}\delta(x - x_{d,i}). \tag{7}$$

On the other hand, the Lagrangian equations governing the evolution of the dispersed droplets are:

$$\frac{dm_d}{dt} = \dot{m}_d, \tag{8}$$

$$m_d \frac{d\boldsymbol{u}_d}{dt} = \boldsymbol{F}, \tag{9}$$

$$m_d c_{p,d} \frac{dT_d}{dt} = \dot{m}_d h_v + A_d h (T - T_d) f', \tag{10}$$

$$\frac{d\boldsymbol{x}_d}{dt} = \boldsymbol{u}_d, \tag{11}$$

where equation (8) describes mass conservation, equation (9) describes momentum conservation, and equation (10) describes energy conservation, whereas equation (11) regulates droplets trajectory.

The right-hand sides of equations (8) to (10) represent the forcing terms and account for droplet evaporation, aerodynamic forces, and convective heat exchange, respectively. The aerodynamic force in equation (9), consisting of the only drag, is expressed through the Schiller-Naumann correlation, i.e., $\boldsymbol{F} = (\boldsymbol{u} - \boldsymbol{u}_d)/(\tau_d)(1 + 0.15Re_d^{0.687})$, to include the effect of the finite droplet Reynolds number Re_d, where $\boldsymbol{u}$ is the carrier phase velocity vector, and $\boldsymbol{u}_d$ and τ_d stand for the droplet velocity and relaxation time, respectively. The mass vaporization rate in equation (8) is written through the Sherwood number Sh, as well as the convective heat exchanged in equation (10) is related to the Nusselt number Nu, i.e., $\dot{m}_d = \pi d_p Sh D_v \rho_v ln(1 + B_m)$, and $h = Nu\alpha_d/d_p$. Here, d_p is the liquid droplet diameter, D_v and ρ_v are the vapor mass diffusivity, and density, k_d denotes the droplet

thermal conductivity, whereas B_m stands for the Spalding mass transfer number. Finally, Sherwood and Nusselt numbers are expressed as a function of the droplet Reynolds number through the Frössling's correlations, i.e., $Sh = 2 + 0.552Re_d^{1/2}Sc^{1/3}$, and $Nu = 2 + 0.552Re_d^{1/2}Pr^{1/3}$, where Sc and Pr denote the molecular Schmidt and Prandtl number, respectively.

Within the same context, the RANS formulation adopts the following governing equations for the carrier phase:

$$\frac{\partial \overline{\rho}}{\partial t} + \frac{\partial (\overline{\rho}\tilde{u}_j)}{\partial x_j} = \overline{S}_m, \tag{12}$$

$$\frac{\partial (\overline{\rho}\tilde{u}_i)}{\partial t} + \frac{\partial}{\partial x_j}\left[\overline{\rho}\tilde{u}_i\tilde{u}_j + \overline{p}\delta_{ij} - \tilde{\tau}_{ij} + \overline{\rho u_i' u_j'}\right] = \overline{\rho} g_i + \overline{S}_{p,i}, \tag{13}$$

$$\frac{\partial \overline{\rho}\tilde{h}_t}{\partial t} + \frac{\partial}{\partial x_j}\left[\overline{\rho}\tilde{h}_t\tilde{u}_j + \tilde{q}_j - \tilde{u}_i\tilde{\tau}_{ij}^{tot}\right] = \frac{\partial \overline{p}}{\partial t} + \rho(\tilde{u}_i g_i) + \overline{S}_e, \tag{14}$$

$$\frac{\partial \overline{\rho}\tilde{y}_k}{\partial t} + \frac{\partial}{\partial x_j}\left[\overline{\rho}\tilde{y}_k\tilde{u}_j + \tilde{J}_j + \overline{\rho}\tilde{u}_j'\tilde{y}_k'\right] = \overline{S}_{m,k}, \tag{15}$$

In the RANS formulation, the "overbar" indicates the Reynolds average, while the "tilde" superscript represents the Favre average ($\tilde{\phi} = \overline{\rho\phi}/\overline{\rho}$). The term $\overline{\rho u_i' u_j'}$ represents the Reynolds stress tensor, which may be modeled employing several closure models, as further discussed in the following.

The RANS and DNS computations are performed through the *sprayFoam* solver supplied within the *OpenFOAM* suite, employing the PIMPLE pressure-based algorithm executed via two inner pressure-velocity corrector loops and three outer PISO corrector loops. Lastly, the solver setup ensures second-order spatial and first-order time accuracy.

Test case configuration

The computations are based on a prototypical configuration, first inquired via DNS to generate reliable reference data, closely resembling the one already investigated by Dalla Barba et al.[16–18] The test case consists of a cylindrical domain filled with air in non-reactive conditions, where a multi-phase acetone-air swirling jet flows out of an orifice of radius $R = 5 \cdot 10^{-3}$ m. Acetone droplets are randomly dispersed through the inflow section, with a uniform initial radius $r_{d,0} = 6$ μm, and locally take on the value of the gaseous carrier velocity on the inflow plane. In this regard, the carrier swirling motion is generated by imposing a Maxworthy inflow profile.[44] In a cylindrical reference frame, in the absence of axial coflow as in the present case, the axial, azimuthal, and radial velocity components are provided by:

$$\begin{cases} U = U_0\left[1 - \frac{1}{2}\left(1 + erf\left(\frac{\tilde{r}-1}{\tilde{\delta}}\right)\right)\right] \\ V = U_0\left[\frac{S_0\tilde{r}}{2}\left(1 - erf\left(\frac{\tilde{r}-1}{\tilde{\delta}}\right)\right)\right] \quad \text{with} \quad \tilde{r} = \frac{r}{R} \quad \text{and} \quad \tilde{\delta} = \frac{\delta}{R} \\ W = 0, \end{cases} \tag{16}$$

where $\tilde{r}$ is the normalized radial distance from the jet axis, S_0 is the so-called swirl rate denoting the slope of the azimuthal velocity at the centreline, α is the core-to-coflow axial velocity ratio, and $\tilde{\delta}$ is the normalized shear layer thickness of the jet.

In the present work, two different swirl levels are investigated, and Table 1 reports the values of the coefficients adopted for the Maxworthy inflow profile in both low-swirl (Case 1) and high-swirl (Case 2) configurations. As may be easily noted, the only distinction between the two test cases is in the swirl rate S_0, directly affecting the azimuthal velocity profile, as illustrated in Figure 1. On the other hand, the axial velocity profile shows no difference among the test cases, with a bulk axial velocity $U_{bulk} = 8.1$ m/s, and is still shown in Figure 1.

Table 1. Maxworthy inflow velocity profile: Values adopted for the axial velocity at the centreline, U_0, swirl rate, S_0, and normalized shear layer thickness of the jet, $\tilde{\delta}$, in the low-swirl (Case 1) and high-swirl (Case 2) configurations. An integral measure of the swirl level is also reported, according to the definition of the swirl number, S, presented in equation (17).

Test case	U_0 [m/s]	S_0 [-]	$\tilde{\delta}$ [-]	S [-]
Case 1	9.25	1.3	0.25	0.54344
Case 2	9.25	1.8	0.25	0.75246

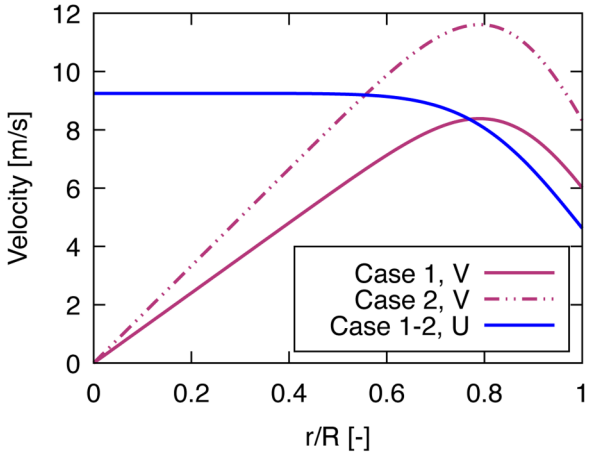

Figure 1. Maxworthy inflow velocity profile: Axial velocity for Case 1 and Case 2 (blue solid line), azimuthal velocity for Case 1 (magenta solid line) and Case 2 (magenta dash-double-dotted line).

Following the definition proposed by Sheen et al.,[45] it is also possible to determine an integral measure of the swirl level arising from the selected Maxhworthy inflow profiles in terms of the swirl number, S, defined as:

$$S = \frac{G_{tg}}{RG_{ax}} = \frac{\int_0^R r^2 UV dr}{R\int_0^R rU^2 dr}, \tag{17}$$

where G_{tg} and G_{ax} represent the tangential and axial momentum fluxes, respectively. In this regard, Table 1 reports the value of S for both Case 1 and Case 2.

The swirling jet discharges in air at ambient pressure, i.e., $p_0 = 101325\ Pa$, whereas the injection temperature is fixed to $T_0 = 273.15\ K$ for both carrier and dispersed phases. The injection flow rate of the gaseous phase is kept constant, fixing a bulk Reynolds number, $Re_0 = 2U_{bulk}R/\nu = 6000$, that corresponds to a configuration of technological interest as concerns swirl-stabilized combustors.[46,47] A nearly-saturated condition is prescribed for the air-acetone vapor mixture at the inflow section, i.e., $S^* = Y_v/Y_{v,s} = 0.99$, where S^* is the saturation, Y_v is the actual vapor mass fraction on the inflow section and $Y_{v,s}(p_0, T_0)$ is the vapor mass fraction in fully-saturated condition, evaluated at the inflow temperature and pressure. The acetone-to-air mass flow rate ratio is set to $\Psi = \dot{m}_{act}/\dot{m}_{air} = 0.28$, with $\dot{m}_{act} = \dot{m}_{act,l} + \dot{m}_{act,v}$ being the sum of liquid and gaseous acetone mass flow rates. The computational domain is characterized by a diameter $D_{dom} = 16R$, and a longitudinal extension $L_{dom} = 25R$, resulting in a fully three-dimensional mesh of 240,000 cells for RANS computations. The resolution of the latter is not established through a grid convergence study; instead, it is derived assuming a fixed computational budget within the framework of a RANS-based preliminary design process of an aeronautical combustion device. On the other hand, the mesh resolution for DNS computations is sufficiently fine (45M grid points) to ensure that the ratio Δ_{DNS}/η_K barely exceeds the value of 3, as illustrated for the low- and high-swirl configurations in Figure 2. In particular, $\Delta_{DNS} = \sqrt[3]{V_{cell}}$ is the average grid element size, with V_{cell} denoting the volume of the generic cell, and $\eta_K = (\nu^3/\varepsilon)^{0.25}$ is the Kolmogorov's length scale. In the latter, ν is the molecular kinematic viscosity, and ε is the turbulence scalar dissipation rate, computed as the trace of the dissipation tensor, $\varepsilon_{ij} = 2\nu\langle\frac{\partial u_i'}{\partial x_k}\frac{\partial u_j'}{\partial x_k}\rangle$, with u_i' indicating the fluctuating velocity in direction i. Lastly, RANS simulations were run until statistical steady-state conditions were attained. In the following, where not expressly stated, QoIs extracted from DNS and RANS computations should be intended as a mean taken over both the tangential direction and time on the Eulerian grid.

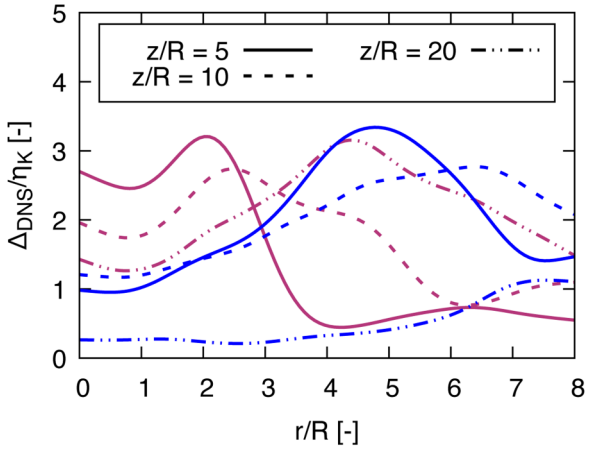

Figure 2. Ratio of DNS mesh element size, Δ_{DNS}, to Kolmogorov's length scale, η_K, for Case 1 (magenta) and Case 2 (blue). The radial distributions at several axial locations are shown.

Preliminary results and model assessment

Direct numerical simulation results

The present section is devoted to illustrating the main physical insights into the low- and high-swirl test case configurations provided by DNS. In particular, as further discussed in the following, the focus is placed on the onset of the VB phenomenon and its fundamental kinematic features. The VB is one of the major phenomena which occur in the presence of swirl under several configurations, among which swirling jets going through an abrupt expansion are typically relevant to aeronautical combustion chamber configurations.

In this regard, Figure 3 reports, on the right side, a graphical visualization of the three-dimensional spatial structure of a bubble-type VB, appearing under Case 1, and a regular conical VB, appearing under Case 2. The coherent vortex structures are visualized through Q-criterion isosurfaces, $Q = 4.0 \times 10^6$, where $Q = \frac{1}{2}(\|\boldsymbol{\Omega}\|^2 - \|\boldsymbol{S}\|^2)$ is the second invariant of the velocity gradient tensor, providing a direct measure of the relative contribution of the mean rotation tensor, $\boldsymbol{\Omega}$, compared with the mean strain tensor, $\boldsymbol{S}$. In particular, the latter does not include the isotropic contribution due to compressibility. As readily evident, Case 1 is characterized by a bubble-type VB, whereas the high-swirl level of Case 2 results in a regular conical VB. This is perfectly consistent with observations in the literature,[35] which highlight the presence of a critical value for the swirl number, S, leading to the formation of a stagnation point and a bubble-type VB. The fundamental effect associated with the critical rotation rate consists in the onset of helical disturbances,[34] which promote the evolution of the jet into a steady helix configuration until the breakdown occurs and a toroidal recirculation zone originates. Moreover, due to the onset of Kelvin-Helmholtz instabilities, the helix is forced to roll up in the streamwise direction, further disorganizing the whole flow pattern. After the onset of the breakdown, any further increase in the

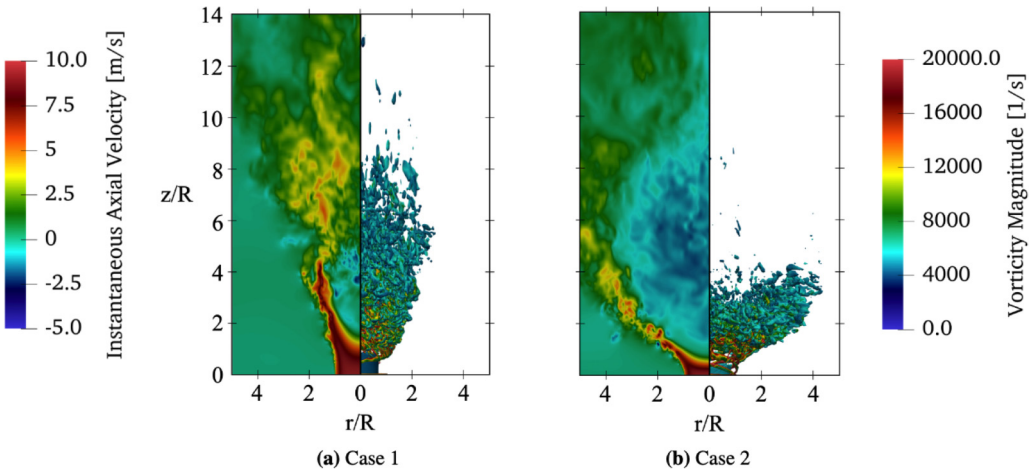

Figure 3. DNS calculations of non-reactive acetone/air spray swirling jet: (a) bubble-type VB, and (b) regular conical VB. On the left, the instantaneous axial velocity field is reported. On the right, coherent vortex structures are visualized employing Q-criterion isosurfaces, $Q = 4.0 \times 10^6$, colored by the vorticity magnitude, $|\omega|$.

swirl level makes the mean location of the stagnation point closer to the nozzle exit,[36,37] which is clearly distinguishable on the left sides of Figure 3, showing the instantaneous axial velocity field for Case 1 and Case 2. The differentiation between the bubble state and the conical state arises during the final stage of the upstream motion of the originated bubble, which transforms into a conical structure due to the presence of internal secondary motions.[34]

Furthermore, the development of the flow pattern downstream of the VB-induced recirculation zone strictly depends on the VB form. As shown in Figure 3(a), under low-swirl conditions, i.e., for Case 1, downstream of the bubble structure, there exists a recovery region, in which the flow results to be more turbulent, the vortex core appears to be expanded[38] compared to the region upstream of the breakdown, and a defect in the axial velocity may be observed, as in typical wakes behind bluff bodies.[34] In particular, although a radial inflow appears in the wake of the bubble, it is of minor importance compared with the radial outflow originating upstream of the recirculation region so that the vortex core is less concentrated in the wake. On the other hand, under high-swirl conditions, i.e., for Case 2, the vortex expansion corresponding to the stagnation point is not followed by any contraction.[34]

Reynolds stresses closure in RANS

If the RANS approach is adopted to capture the kinematic features associated with a swirling jet undergoing VB, selecting a closure model for the Reynolds stresses and calibrating the embedded parameters are of paramount importance.[48,49]

Within the framework of the Reynolds-averaged approach, it is possible to rank the existing closure models based on their ability to capture the dynamics of each Reynolds stress component. Following these considerations, a preliminary analysis is performed to estimate the most suitable closure model for Reynolds stresses to be adopted, given the flow configurations under examination. This is accomplished through the numerical analysis of two single-phase swirling jets, still characterized by the Maxworthy profiles reported in Table 1, adopting a variety of Reynolds stresses closure models which are briefly recalled in the following. Lastly, these RANS computations are performed on a restricted portion of the original domain, corresponding to a 5° wedge axisymmetric mesh configuration. A detailed comparison between RANS and DNS calculations focused on the velocity field is discussed in the following.

Table 2. Modeling of eddy viscosity production according to different forms of the Spalart-Allmaras model: Ω_{ij} is the mean rate-of-rotation tensor, S_{ij} is the mean rate-of-strain tensor, and U_{ij} is the velocity gradient tensor. The following notation is adopted: $|\Omega_{ij}| = \sqrt{2\Omega_{ij}\Omega_{ij}}$, $|S_{ij}| = \sqrt{2S_{ij}S_{ij}}$, and $|U_{ij}| = \sqrt{2U_{ij}U_{ij}}$.

SA-1	SA-2	SA-3
$J = \sqrt{2\Omega_{ij}\Omega_{ij}}$	$J = \sqrt{2S_{ij}S_{ij}}$	$J = \sqrt{2U_{ij}U_{ij}}$
SA-4		
$J = \lvert\Omega_{ij}\rvert + C_{prod} \cdot \min(0, \lvert S_{ij}\rvert - \lvert\Omega_{ij}\rvert)$		

One-Equation models. The most commonly employed one-equation model refers to the one proposed by Spalart and Allmaras,[50] which solves a transport equation for a modified form of the turbulent kinematic viscosity, i.e., $\tilde{\nu}$. Within the latter, a leading role is played by the production term of the turbulent viscosity, i.e., $G_\nu = \rho C_{b1} \tilde{S} \tilde{\nu}$, where $C_{b1} = 0.1355$ is an empirically calibrated parameter and $\tilde{S}$ strictly depends on a scalar J. Depending on the form of J, it is possible to identify four variants of the Spalart-Allmaras model, illustrated in Table 2. In particular,

the SA-4 model tends to locally limit the production of eddy viscosity where the vorticity measure overcomes the strain rate, with the C_{prod} parameter set to 2.[51]

Nevertheless, under low-swirl conditions, i.e., for Case 1, none among the four variants of the Spalart-Allmaras model predicts the onset of a reverse flow region, as evident from Figure 4(a)(d). On the other hand, under high-swirl conditions, i.e., for Case 2, the extension of the VB-induced recirculation zone is largely underestimated by each model, and a bubble-type VB is captured by the *SA-4* model instead of the regular conical form, see Figure 5(a)(d).

Two-Equation models. A higher level of Reynolds stresses closure is, in principle, provided by two-equation models (TEMs). In particular, the focus is here placed on four different models, namely, the $k-\varepsilon$ model,[52] hereinafter denoted as kEps, the realizable $k-\varepsilon$ model,[53] hereinafter denoted as kEps – re, the RNG $k-\varepsilon$ model in its high-Reynolds number formulation,[54] hereinafter denoted as kEps – RNG, and a non-linear two-equation closure model proposed in,[55] hereinafter denoted as NLEVM.

Under low-swirl conditions, i.e., for Case 1, the NLEVM model is the only one able to capture the onset of a bubble-type VB form, see Figure 4(h), whereas the remaining models do not predict any reverse flow. This may be ascribed to a non-linear stress–strain relationship, which transcends the Boussinesq hypothesis typically employed within linear eddy viscosity models. Therefore, the NLEVM is selected as one of the closure models by which Case 1 will be further investigated in a fully three-dimensional configuration in the following. On the other hand, under high-swirl conditions, i.e., for Case 2, all the models, except for the kEps – re, predict a regular conical VB form. In particular, the kEps – RNG model exhibits the most appreciable predictive accuracy compared with DNS data, as shown in Figure 5(g). It is thus selected as one of the closure models by which Case 2 will be further investigated in a fully three-dimensional configuration in the following. Such a model is equipped with an additional term in the transport equation for the turbulence scalar dissipation rate, ε, compared to the standard kEps model, which provides a decrease in the destruction of ε within regions of large strain.

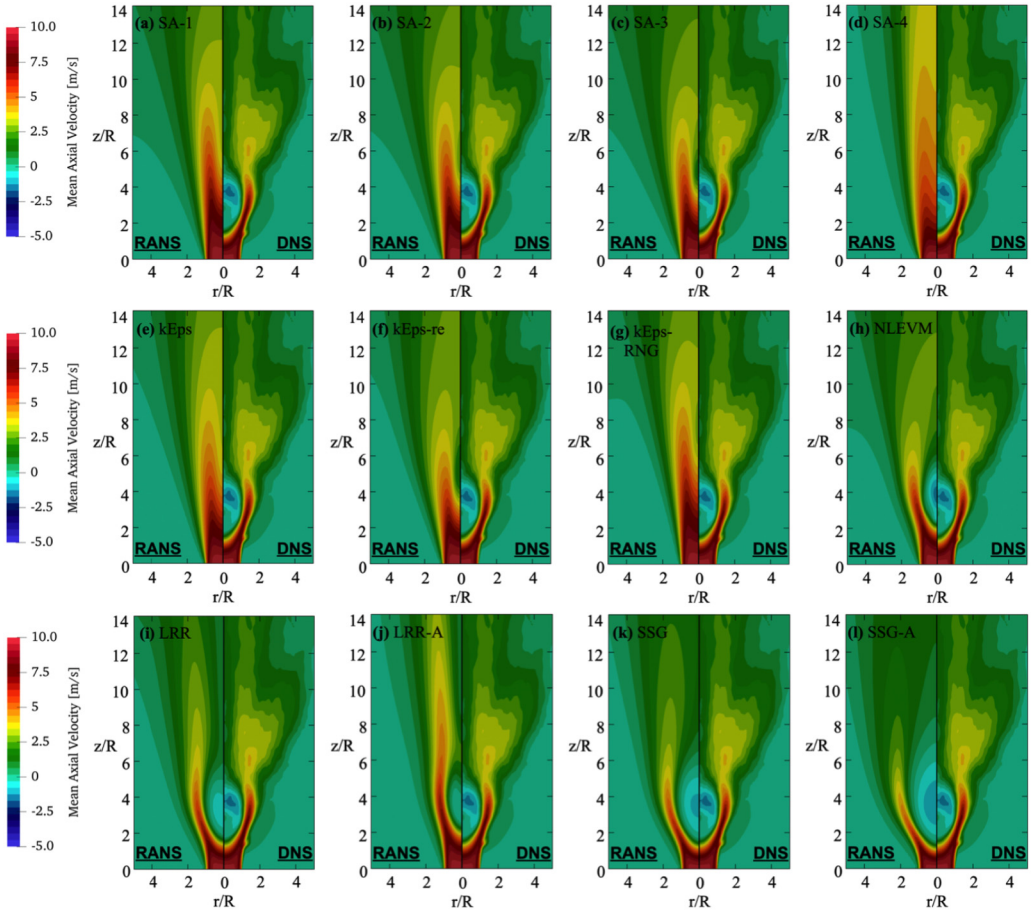

Figure 4. Case 1, preliminary analysis on Reynolds stresses closure: Mean axial velocity field provided by axisymmetric RANS (left) and DNS (right). RANS: Reynolds-averaged NavierStokes; DNS: direct numerical simulation.

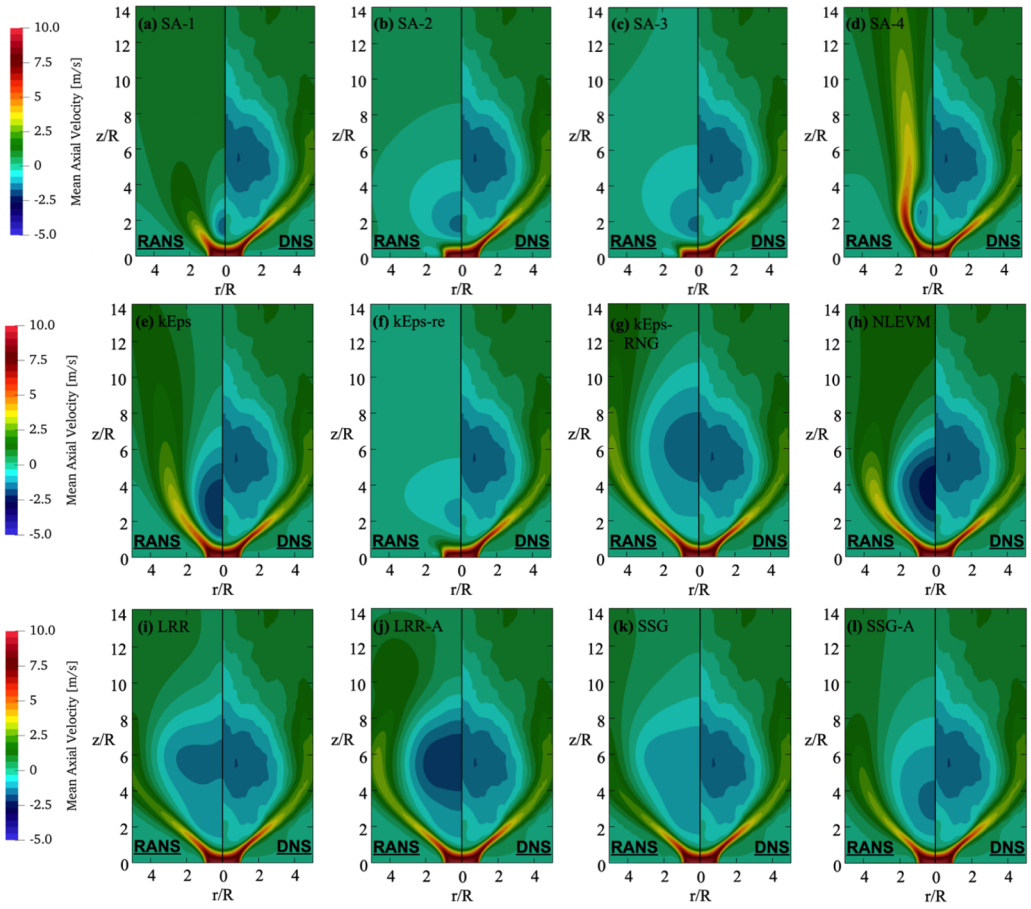

Figure 5. Case 2, preliminary analysis on Reynolds stresses closure: mean axial velocity field provided by axisymmetric RANS (left) and DNS (right). RANS: Reynolds-averaged NavierStokes; DNS: direct numerical simulation.

Second-Moment closure models. Within the Reynolds-averaging approach, second-moment closure (SMC) models represent the natural—and highest—level of modeling turbulent flows, enabling to develop model sensitivity to the orientation of turbulence structure and anisotropy of normal stresses, as well as account for extra-strain deriving from streamline curvature and system rotation, as an example.[56] Even in this case, four different closure models are tested; namely, the Launder-Reece-Rodi model,[57] hereinafter denoted as LRR, the Launder–Reece–Rodi model adopting an anisotropic treatment of the dissipation tensor ε_{ij} as suggested by Rotta,[58] hereinafter denoted as LRR-A, the Speziale-Sarkar-Gatski model,[59] hereinafter denoted as SSG, and the Speziale-Sarkar-Gatski model including an algebraic anisotropic dissipation rate model,[60] hereinafter denoted as SSG-A.

Under low-swirl conditions, i.e., for Case 1, all the models capture the onset of a bubble-type VB form, see Figure 4-(l). On the other hand, under high-swirl conditions, i.e., for Case 2, all the models can reproduce a regular conical VB-induced recirculation region, as evident in Figure 5(i) to (l). Given these considerations, in the following, both Case 1 and Case 2 will be further investigated in a fully three-dimensional configuration utilizing the LRR model. Although the anisotropy degree of the turbulence dissipation rate tensor should be, in principle, addressed in VB-affected swirling flows,[61] anisotropic closure models tested in the present work do not show any improvement compared with the classical formulation of the LRR model. Therefore, it is here decided to adopt a fully isotropic treatment of the dissipation tensor. In contrast, a deeper investigation of the link between the most relevant features of ε_{ij} and the local flow conditions is postponed to future works.

Selection of sub-grid models

As further discussed in the following section, the present work considers two different sources of uncertainty about RANS computations, dealing with the spray dispersion model and the turbulent Schmidt number. Indeed, while the correct reproduction of liquid droplet dispersion is crucial to reconstruct the spray structure accurately,[15] the

selection of the turbulent Schmidt number is reported to deeply affect the temperature field in a diffusive combustion system.[62]

The starting point is represented by an adequate selection of such models, which is proposed below.

Liquid droplet dispersion model

Within the RANS approach, turbulent fluctuations are not directly resolved. Hence, liquid droplets would be exclusively influenced by the mean velocity field, thus introducing a dispersion model is unavoidable for a satisfactory reconstruction of the Eulerian velocity field influence over the droplet position. The dispersion model estimates the velocity component $\boldsymbol{u}'$, related to the unresolved fluctuations. Two different turbulent particle dispersion models are explored in this work: (a) discrete random walk (DRW),[63] (b) gradient-based dispersion. Following the work of Mueller and Raman,[43] the velocity oscillation is defined through a blending of the aforementioned dispersion models by introducing a blending coefficient, ω_d:

$$\boldsymbol{u}' = (1 - \omega_d)\boldsymbol{u}'_{DRW} + \omega_d \boldsymbol{u}'_{\nabla}. \tag{18}$$

Turbulent schmidt number

The turbulent Schmidt number Sc_t plays a crucial role in the transport and diffusion of the acetone vapor mass fraction by directly affecting the mass diffusivity, i.e., the diffusive term J_j appearing in equation (15). In particular, if a constant Schmidt number assumption is pursued, there is much uncertainty about the correct value of Sc_t having to be assigned.[64,65] On the other hand, several variable Schmidt and Prandtl number models have been proposed,[66–69] although each is formulated and calibrated concerning specific fields of applications. In particular, Xiao et al.[66] derived a complete turbulence model which accounts for variable turbulent Prandtl, Pr_t, and Schmidt, Sc_t, numbers relying on the introduction of additional transport equations for the variance of enthalpy and concentrations and their dissipation rates. Although the model was successfully tested against experiments involving supersonic mixing and combustion,[67] formulating additional transport equations requires ad hoc calibration of a large number of modeling constants based on the test case under consideration. Conversely, Goldberg et al.[68] proposed a fully algebraic formulation to approximate the spatial distribution of Pr_t and Sc_t, which merely takes into account the chemical species characterized by the maximum gradient at a specific location in the case of a multi-species flow test case. Lastly, Longo et al. formulated a data-driven model for Sc_t for RANS approaches employing high-fidelity delayed detached eddy simulation about atmospheric dispersion, in combination with principal component analysis. Given these considerations, it is here decided to adopt a constant Schmidt number model to assess the sensitivity of the vapor mass fraction field to the selection of a suitable value for Sc_t, which is the primary focus of the present work. Nonetheless, as a future research work, we intend to exploit the high-fidelity DNS dataset at our disposal to determine the spatial distribution of Sc_t in the configurations of interest so as to eventually adopt a Bayesian inference approach to formulate an ad hoc variable Schmidt number model addressing VB flow conditions.

Bayesian framework for uncertainty quantification

The present work investigates how the uncertainty associated with model parameters propagates to the QoIs, adopting a Bayesian setting.

Supposing the PDFs of the uncertain parameters are known, the most straightforward approach would be to sample values of such parameters and obtain the corresponding values of the QoIs via RANS computations in a Monte Carlo fashion. If a sufficiently large number of samples is produced, converged statistics of the QoIs may be computed. However, the convergence rate of the Monte Carlo methods with the number of samples is notoriously slow: to accurately characterize the statistical properties of the QoIs, the procedure described above requires a large number of samples, typically of the order of thousands, each requiring a RANS computation. This issue can be circumvented by assuming a certain degree of smoothness in the QoIs statistics and resorting to a non-intrusive spectral projection technique employing a PCE representation of the uncertain variables.

Indeed, a PCE provides a valuable means for propagating uncertainty as an alternative to classical Monte Carlo methods and allows for efficient propagation of uncertainty in computational models and a straightforward assessment of the output variance sensitivity to each component of the uncertain input vector, $\boldsymbol{\lambda} = (\lambda_1, .., \lambda_{n_s})$, with n_s being equal to the number of stochastic degrees of freedom. The uncertain input parameters can be written as a function of independent identically distributed (i.i.d.) standard RVs, ξ_i. Hence $\boldsymbol{\lambda} = \boldsymbol{\lambda}(\boldsymbol{\xi})$, where $\boldsymbol{\xi} = (\xi_1, .., \xi_{n_s})$ is the random *germ*. Being the generic QoI, $\boldsymbol{y}$, the function of the input parameters through the computational model, it also depends on the RVs $\boldsymbol{\xi}$, so that $\boldsymbol{y} = \boldsymbol{y}(\xi_1, .., \xi_{n_s})$. Then, a PCE may provide a spectral representation of the RV $\boldsymbol{y}(\boldsymbol{\xi})$ as:

$$\boldsymbol{y} \simeq \sum_{\beta \in J} y_\beta \boldsymbol{\Psi}_{\boldsymbol{\beta}}\left(\xi_1, \ldots, \xi_{n_s}\right), \tag{19}$$

where $\boldsymbol{\beta} = (\beta_1, \ldots, \beta_{n_s})$, $\forall \beta_j \in \mathbb{N}_0$, is a multi-index, and $\boldsymbol{\Psi}_\beta$ are multivariate normalized orthogonal polynomials written as products of univariate orthonormal polynomials ψ_β:

$$\mathbf{\Psi}_\beta(\xi_1, \ldots, \xi_{n_s}) = \prod_{j=1}^{n_s} \psi_{\beta_j}(\xi_j). \quad (20)$$

The PCE is typically truncated at degree N multivariate polynomials so that the expansion comprises $(n_s + N)!/(n_s!N!) - 1$ terms in equation (19).

The univariate functions ψ_β are polynomials of degree β_j in the independent variable ξ_j and are orthonormal with respect to the density of the RV ξ_j, such that:

$$\mathbb{E}[\psi_k(\xi_j)\psi_n(\xi_j)] = \int \psi_k(\xi_j)\psi_n(\xi_j)p(\xi_j)d\xi_j = \delta_{k,n}. \quad (21)$$

The coefficients y_β are the expansion coefficients obtained by Galerkin projection. As an example, the y_β are defined as:

$$y_\beta = \mathbb{E}\big[y(\lambda)\psi_\beta\big] = \int y(\lambda(\xi))\psi_\beta(\xi)p(\xi)d\xi. \quad (22)$$

Moreover, the PCE approach brings the possibility to compute the output variance and sensitivity indices as follows:

$$\mathrm{Var}[y(\xi)] = \sum_{\beta>0}^{N} y_\beta^2 <\psi_\beta, \psi_\beta>, \quad (23)$$

$$S_i = \frac{1}{\mathrm{Var}[y(\xi)]} \sum_{\beta \in J_i}^{N} y_\beta^2 <\psi_\beta, \psi_\beta>, \quad (24)$$

where $J_i = \{\beta \in J : \beta_i > 0, \beta_k = 0, k \neq i\}$.

It should be stressed that, once the proper basis $\mathbf{\Psi}$ is chosen, the computation of the coefficients y_β from equation (22) allows one to fully characterize the uncertain output $\boldsymbol{y}$. In this work, the expansion coefficients are calculated by resorting to a quadrature technique that aims at approximating the integral in equation (22) with the knowledge of $\boldsymbol{y}(\boldsymbol{\lambda}(\xi_i^Q))$, where ξ_i^Q are the quadrature points.

Once the QoIs expansions are determined from equation (19), the inexpensive sampling of the germ $\boldsymbol{\xi}$ results in the opportunity to explore the probability distribution of the QoIs, also known as *pushforward distribution*, induced by the assumed probability density on model parameters, and visualize the associated credible interval. The latter is calculated using the high posterior density interval (HPDI) methodology.

Uncertain input parameters

In the present case, two uncertain input parameters are identified and assigned specific probability distributions based on the authors' knowledge and available literature. In this respect, it may be worth recalling that if an inverse UQ analysis is performed, PDFs of the input parameters are calibrated from data and ready to undergo forward uncertainty propagation.

The first source of uncertainty arises from selecting the liquid droplet dispersion model. Going into detail, any combination of the DRW and gradient-based dispersion model is assumed to be equally plausible. Therefore, the blending coefficient, ω_d, is presumed to be uniformly distributed in the range 0-1, i.e., $\omega_d \sim \mathcal{U}(0, 1)$, letting the dispersion model vary from purely gradient-based to purely stochastic, and is then parametrized as a function of the standard RV $\xi_1 \sim \mathcal{U}(-1, 1)$. Concerning the turbulent Schmidt number, Sc_t, a uniform distribution in the range 0.2–1.0 is considered. Therefore, Sc_t is parametrized as a function of the standard RV $\xi_2 \sim \mathcal{U}(-1, 1)$.

Gauss-Legendre quadrature nodes

Once the probability distributions for the uncertain input parameters have been chosen, as summarized in Table 3, the integral in equation (22) needs to be approximated by exploiting the quadrature points ξ_i^Q associated with the standard RVs.

Within this context, it is worth recalling that Legendre polynomials are mutually orthogonal with respect to the density of uniform probability measure, which characterizes both the ξ_1 and ξ_2 standard RVs. Given these considerations, the adoption of a second-order tensor-product Gauss-Legendre quadrature rule discretizes the sample space in 3 nodes for each standard RV, for a total of 9 quadrature points.

Nonetheless, a sparse grid can be constructed from a product of one-dimensional Gauss-Legendre rules to alleviate the computational burden associated with multidimensional quadrature. In particular, Smolyak's procedure offers a way to build a sparse grid of comparable precision with the tensor-product one by exploiting a weighted sum of lower-order product rules.[70] For a d-dimensional uncertain input space, a Smolyak's sparse quadrature set of level l is defined as:

$$S_k^{(d)} f = \sum_{q=l-d}^{l-1} (-1)^{l-1-q} \binom{d-1}{l-1-q} \times \sum_{\|\boldsymbol{k}\|_1 = q+d} Q_{2^{k_1}-1} \otimes \cdots \otimes Q_{2^{k_d}-1} f, \quad (25)$$

where $\|\boldsymbol{k}\|_1 = \sum_{i=1}^{d} |k_i|$, and $Q_{2^{k_i}-1}$ is the k_{1i}-th order base

Table 3. Uncertain input parameters: standard RVs, existence domain, and quadrature rule.

Uncertain input	Standard RV	Parameter range	Quadrature rule
ω_d	$\xi_1 \sim \mathcal{U}(-1, 1)$	$\omega_d \in [0, 1]$	Gauss-Legendre
Sc_t	$\xi_2 \sim \mathcal{U}(-1, 1)$	$Sc_t \in [0.2, 1]$	Gauss-Legendre

quadrature rule, namely, the Gauss-Legendre rule in the present case.

Here, it is decided to adopt a second-level Smolyak's sparse grid, i.e., $l = 2$, which results in a total of 5 quadrature points, compared with the 9 quadrature points returned by the tensor-product Gauss-Legendre rule.

Results and discussion

The present section illustrates the results obtained utilizing a forward UQ analysis performed on both low- and high-swirl configurations. In particular, as already stated, Case 1 was investigated through NLEVM and LRR closure models, whereas Case 2 was investigated through kEps-RNG and LRR closure models.

Main observables and error bars

A truncated order-3 PCE representation of the most relevant QoIs within the non-reactive configuration under scrutiny, i.e., the velocity field $\boldsymbol{U}(\boldsymbol{\xi}, \boldsymbol{x})$, and the acetone vapor mass fraction field $Y_v(\boldsymbol{\xi}, \boldsymbol{x})$, is constructed within each element of the computational domain employing the RANS solutions obtained in the Gauss quadrature nodes. In turn, the random sampling of the random germ $\boldsymbol{\xi}$ in the PCEs returns the opportunity to get the corresponding PDFs via kernel density estimation (KDE), and consequently, the mean and the variance of the selected QoIs, as well as their confidence intervals. In particular, it was assumed that the 75% confidence interval constitutes a meaningful measure of the degree of belief about the QoIs.

Case 1. The variability of the velocity vector field is first discussed as concerns Case 1. First, the forward propagation of model uncertainty induces almost no variance in the velocity field. The uncertainty band remains extremely narrow in the entire computational domain, except for isolated instances, where the variability of the radial velocity, W, can be ascribed to the influence locally exerted by the droplet dispersion model in terms of gas-liquid momentum exchange. Therefore, it is decided to focus exclusively on the pushforward mean velocity field. In this regard, Figure 6 shows the pushforward mean axial, azimuthal, and radial velocity fields, compared with the DNS mean velocity field. As concerns the predictive accuracy of the turbulence closure models under examination, on the one hand, the LRR model shows an overall agreement in terms of axial and azimuthal velocity components compared with DNS data. On the other hand, the LRR model underestimates the reverse flow intensity within the VB-induced recirculation region, as evident in Figure 6(a). Moreover, almost no radial motion in the wake of the bubble, i.e., from $z/R = 4$ on, is captured. In this regard, DNS data show a significant radial inflow in the recovery region, and then a slightly pronounced jet spreading, see Figure 6(c), which the LRR model again slightly underestimates. Nonetheless, the LRR model proves to adequately reproduce entrainment velocity, see Figure 6(c), as well as the wake-like behavior in the recovery region, characterized by centreline speeds lower than those outside the vortex core, see Figure 6(a). Conversely, the results provided by the NLEVM closure model are globally in worse agreement with DNS data. In particular, the

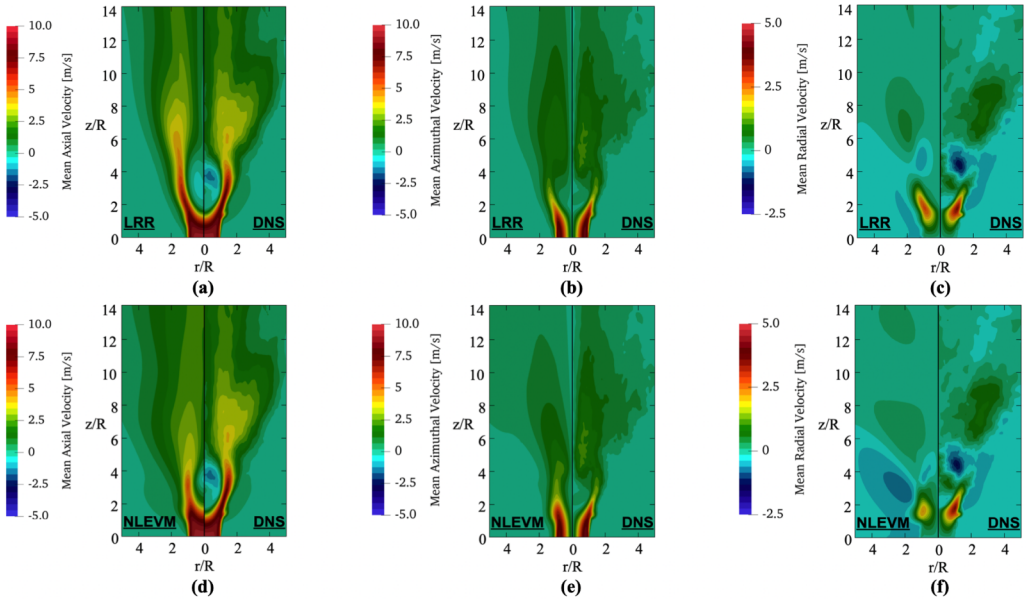

Figure 6. Case 1, pushforward mean velocity components (left), compared with the DNS mean velocity field (right). Top line, LRR model: (a) axial velocity, (b) azimuthal velocity, and (c) radial velocity. Bottom line, NLEVM model: (d)-(f) labeled as (a)-(c). LRR: Launder-Reece-Rodi; DNS: direct numerical simulation.

NLEVM model predicts the onset of the stagnation point upstream of the location indicated by DNS, see Figure 6(d), and the axial extension of the central recirculation zone is considerably underestimated. More in general, the predictive capability of the NLEVM model in terms of axial and azimuthal velocity components is quite unsatisfactory, see also Figure 6(e). Furthermore, the NLEVM model barely reproduces the radial motions in the bubble's surroundings highlighted by DNS data, see Figure 6(f).

Concerning the variance of the acetone vapor mass fraction, Y_v, Figure 7 reports the radial distributions of Y_v, normalized by the fully-saturated mass fraction evaluated at the inflow conditions, $Y_{v,s}(T_0, p_0)$, along with the associated 75% credible interval calculated via the HPDI approach. In this case, the forward propagation of model uncertainty induces significant variance in the acetone mass fraction field, regardless of the closure model adopted. Similar to what was already observed concerning the velocity field, the LRR model shows superior agreement with DNS data compared to the NLEVM model. The latter tends to underpredict Y_v inside the vortex core region, i.e., approximately for $r/R \leq 2$. In contrast, the pushforward mean distribution of Y_v provided by the LRR model is in close agreement with DNS results. Regarding the vapor mass fraction variability, in the near-field region, i.e., up to $z/R = 2$, most of the output variance is concentrated within the mixing layer, i.e., close to $r/R = 2$. On the other hand, downstream of the VB-associated stagnation point, i.e., approximately from $z/R = 4$ on, the variability of Y_v is particularly evident within both the vortex core region and the entrainment-affected region. At the same time, almost no output variance can be envisaged in the shear layer, where the credibility interval virtually vanishes.

This is corroborated by the global variance-based sensitivity analysis performed within the Bayesian framework, the outcome of which is presented in Figure 8 in case the LRR model is adopted. In this regard, remarking that no substantial difference may be qualitatively envisaged in case the NLEVM model is employed, Figure 8(a) shows a comparison between the pushforward mean field of Y_v (on the left), obtained by sampling the random germ $\boldsymbol{\xi}$ in the PCEs, and the variance of Y_v (on the right), as computed from equation (23) for each PCE-based surrogate model. Moreover, the pushforward mean field of Y_v is featured with the mean velocity field streamlines (solid black lines), calculated from the pushforward mean distributions of U, V, and W, so that the VB-associated stagnation point and the central recirculation zone may be clearly distinguished. Thanks to this graphical representation, it is possible to identify the near-field mixing layer and the far-field vortex core as those regions where the variance of Y_v is mostly concentrated. Furthermore, Figure 8(b) and (c) show the field distribution of the first-order, or main-effect, Sobol' sensitivity indexes for the dispersion blending coefficient, ω_d, and the turbulent Schmidt number, Sc_t, respectively, concerning the contribution of each uncertain input to the variability of Y_v, as computed from equation (24). As can be observed, except for a limited region in proximity of the inflow section, the droplet dispersion model

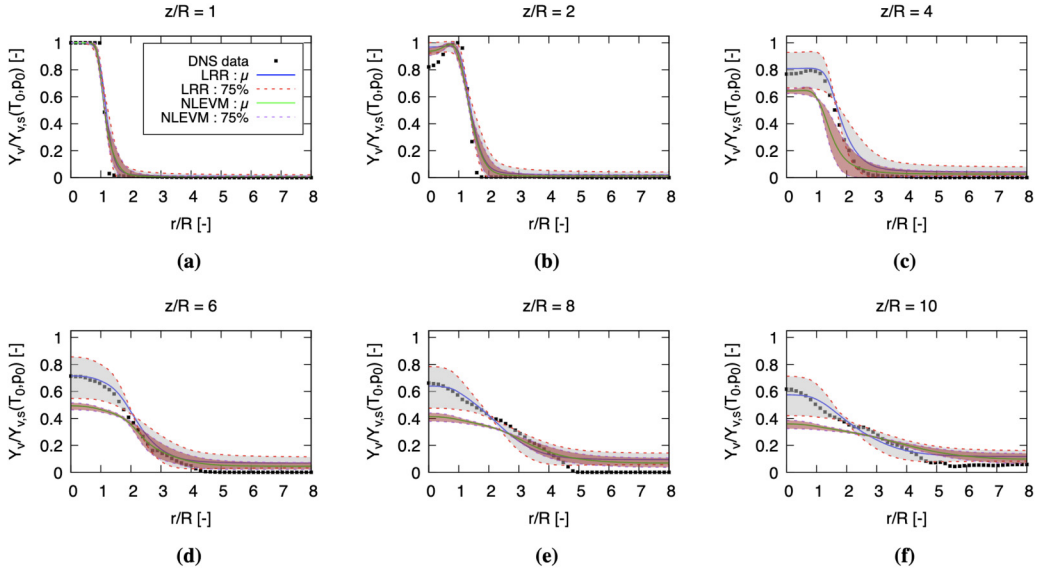

Figure 7. Case 1, radial distribution of the mean acetone vapor mass fraction, Y_v, normalized by the vapor mass fraction in fully saturated condition and accompanied with the 75% credible interval. Top line, from left to right: (a) z/R = 1, (b) z/R = 2, (c) z/R = 4. Bottom line, from left to right: (d) z/R = 6, (e) z/R = 8, (f) z/R = 10. Red (purple) dashed lines encompass a gray (brown) region, representing the credible interval, and the blue (green) solid line depicts the mean value distribution returned by the Launder–ReeceRodi (LRR) (NLEVM) closure model.

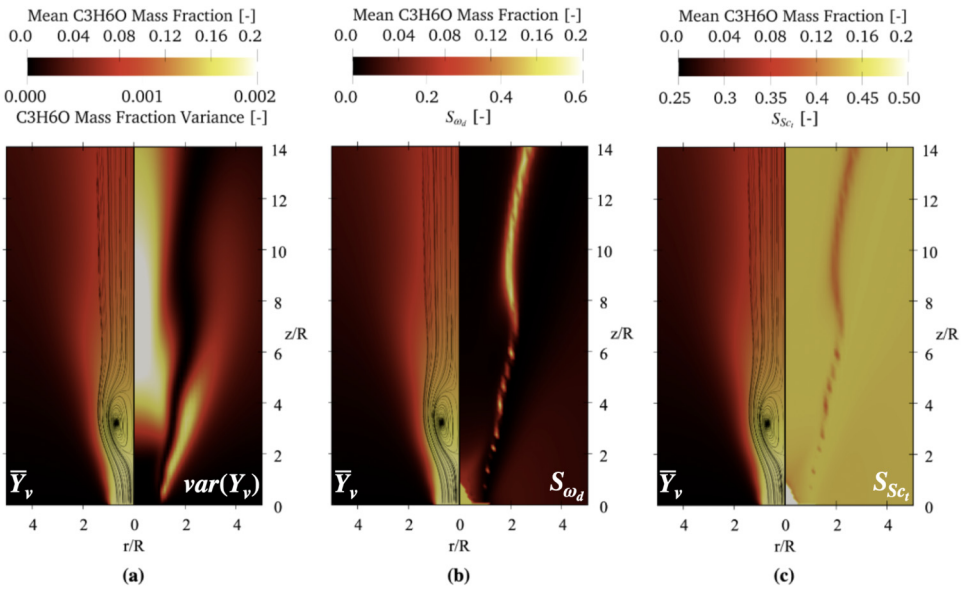

Figure 8. Case 1, variance-based sensitivity analysis of the mean acetone vapor mass fraction, Y_v, via Launder–Reece–Rodi (LRR) model: (a) pushforward mean of Y_v (left) VS variance (right) of Y_v, as computed from equation (23), (b) pushforward mean of Y_v (left) VS Sobol index of the dispersion model blending coefficient, S_{ω_d}, as computed from equation (24) (right), (c) pushforward mean of Y_v (left) VS Sobol index of the turbulent Schmidt number, S_{Sc_t} (right). The pushforward mean velocity field streamlines (solid black lines) are overlapped with the color map of the push forward means of Y_v.

exclusively plays a role in the far-field mixing layer, which is characterized by an overall vanishing output variance, see Figure 8(a). Therefore, this hints that the field distribution of acetone vapor mass fraction is slightly affected by the choice of the droplet dispersion model, which can be regarded as a *second-class* uncertainty. Conversely, as shown in Figure 8(c), the turbulent Schmidt number offers a significant contribution to the overall variance of Y_v in the entire computational domain, including those regions where the variability of the acetone vapor mass fraction is most evident, namely, the near-field shear layer and the far-field vortex core.

Case 2. Moving onto the high-swirl configuration, i.e., Case 2, given that the forward propagation of model uncertainty does not induce any variance in the velocity field also in this case, Figure 9 illustrates the pushforward mean velocity components compared with the DNS mean velocity field. Regarding the predictive accuracy of the turbulence closure models under examination, the LRR model again shows an overall agreement with the velocity components provided by DNS, reflecting that such a closure model represents the most versatile approach among the RANS models when addressing different VB states. Nevertheless, as may be observed from Figure 9(a), the LRR model slightly underpredicts the size of the VB-induced recirculation region, which is reported to extend approximately up to $r/R = 2$ and $z/R = 8$, in the radial and axial directions, respectively, within the Reynolds-averaging approach. This aspect is strictly associated with the discrepancies in the prediction of the radial velocity by the LRR model; see Figure 9(c). In fact, due to the smaller extension of the recirculation zone predicted by the LRR model, a negative radial motion already occurs at $z/R = 6$. In contrast, DNS results still show a spreading of the jet. On the other hand, the kEps-RNG correctly predicts the axial and radial extension of the VB-induced recirculation zone, see Figure 9(a). This is accompanied by a closer agreement between RANS and DNS results as concerns the radial velocity field as well, see Figure 9(c). However, the kEps-RNG model is characterized by the poorer predictive capability of the axial velocity component surrounding the final part of the recirculation zone, which is overestimated, as again evident in Figure 9(a).

Concerning the acetone vapor mass fraction, Y_v, Figure 10 reports the radial distributions of Y_v, normalized by the fully-saturated mass fraction evaluated at the inflow conditions, $Y_{v,s}(T_0, p_0)$, along with the associated 75% credible interval. Similarly to what was already observed concerning the velocity field, the kEps-RNG model shows superior agreement with DNS data compared to the LRR model. The latter tends to overpredict Y_v inside the vortex core region, which extends up to approximately $r/R = 5$ in the far field. In contrast, the pushforward mean distribution of Y_v provided by the kEps-RNG model is in closer agreement with DNS results, especially in the proximity of the shear layer. At the same time, the kEps-RNG still overpredicts the acetone vapor mass fraction in the near-axis region, albeit to a lesser extent than the LRR model.

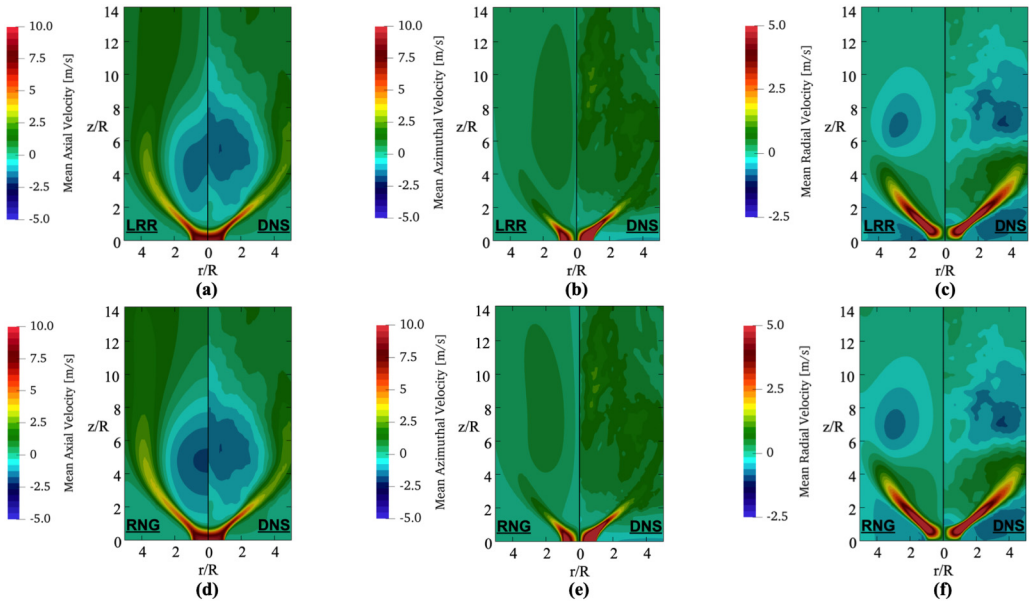

Figure 9. Case 2, pushforward mean velocity components (left), compared with the DNS mean velocity field (right). Top line, LRR model; bottom line, kEps-RNG model: (a)-(f) as labeled in Figure 6. DNS: direct numerical simulation; LRR: Launder–Reece–Rodi.

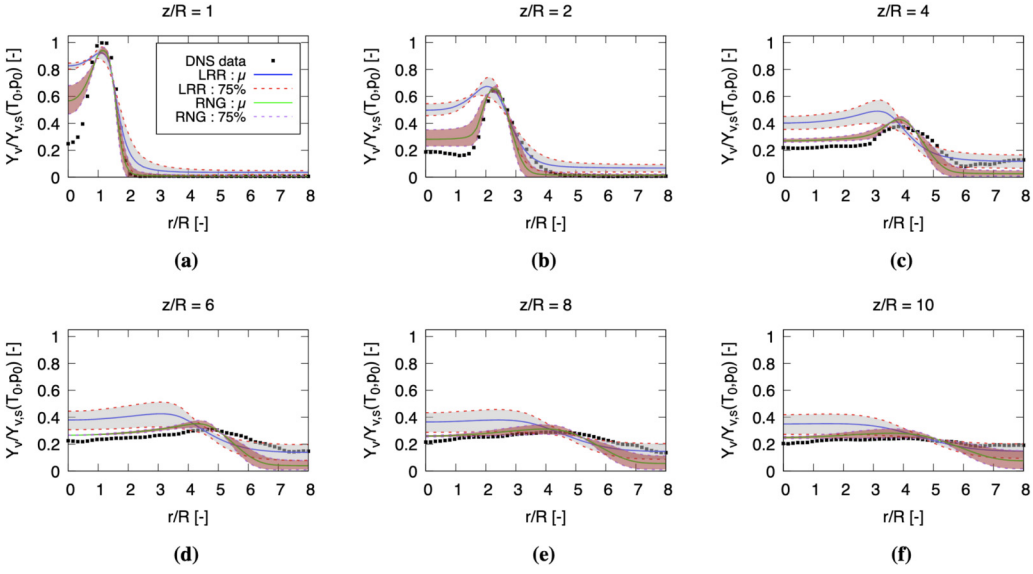

Figure 10. Case 2, radial distribution of the mean acetone vapor mass fraction, Y_v, normalized by the vapor mass fraction in fully saturated condition, and accompanied with the 75% credible interval via Launder–Reece–Rodi (LRR) and kEps-RNG models: (a)–(f) as labeled in Figure 7.

In both cases, DNS data do not fall within the 75% confidence interval returned by the forward UQ analysis, thus highlighting the inability of the RANS approach to recover Y_v values provided by DNS, given the adopted probability distributions for the uncertain model parameters. Lastly, the LRR model performs better than the kEps-RNG model outside the vortex core region. Since the uncertainty band does contain the entirety of DNS data, a proper choice of ω_d and Sc_t may result in a correct reproduction of the acetone vapor mass fraction field by the LRR model in such a region. Regarding the vapor mass fraction variability, also for Case 2, in the near-field region, i.e., up to $z/R = 2$, most of the output variance is concentrated within the mixing layer, i.e., close to $r/R = 1 - 2$. On the other hand, downstream of the VB-associated stagnation point, i.e., approximately from $z/R = 4$ on, the variability of Y_v is particularly evident within the outer zone of the recirculation region and the

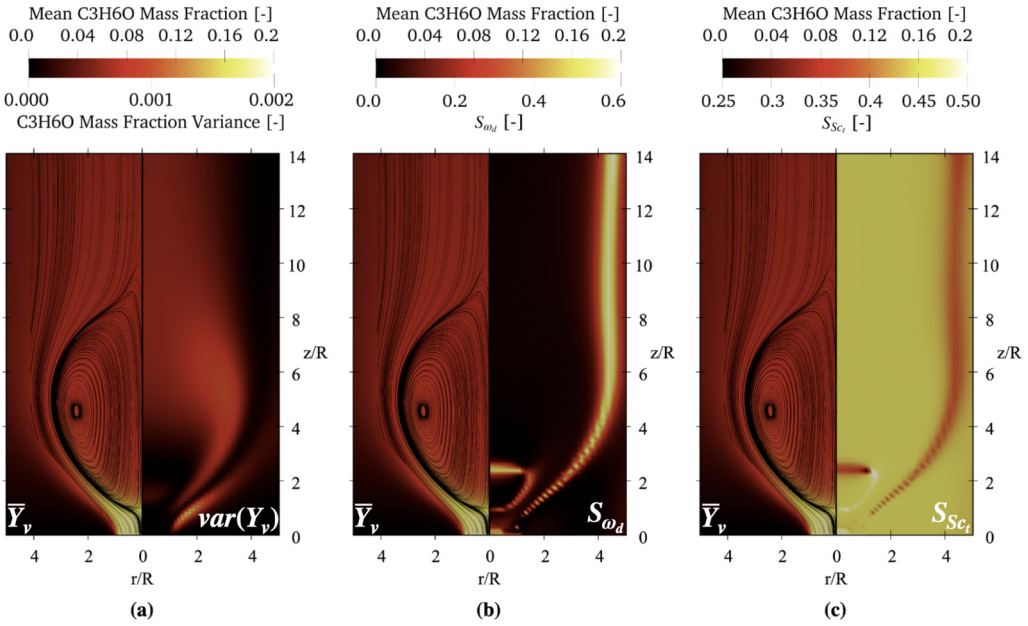

Figure 11. Case 2, variance-based sensitivity analysis of the mean acetone vapor mass fraction, Y_v, referred to the Launder–ReeceRodi (LRR) model: (a)–(c) as labeled in Figure 8.

region beyond the mixing layer. At the same time, almost no output variance can be envisaged in the shear layer, where the credibility interval virtually vanishes.

This is again corroborated by the outcome of the Bayesian-based global sensitivity analysis for the LRR model, as shown in Figure 11. In particular, Figure 11(a) depicts the variance of Y_v, as computed from equation (23), denoting the near-field mixing layer and the outer zone of the VB-induced recirculation region as areas where the variance of Y_v is greatly concentrated. Moreover, Figure 11(b) and (c) show the field distribution of the Sobol' sensitivity indexes for ω_d and Sc_t, respectively, concerning the contribution of each uncertain input to the variability of Y_v, as computed from equation (24). As can be observed, also for Case 2, the droplet dispersion model exclusively plays a role in the far-field mixing layer, characterized by an overall vanishing output variance, see Figure 11(a). Therefore, this hints that also under high-swirl conditions the field distribution of acetone vapor mass fraction is slightly affected by the choice of the droplet dispersion model, which can be regarded again as a *second-class* uncertainty. Conversely, as shown in Figure 11(c), the turbulent Schmidt number offers a significant contribution to the overall variance of Y_v in the entire computational domain, including those regions where the variability of the acetone vapor mass fraction is most evident.

Liquid-phase conditional-probability local analysis

To further assess the role played by the dispersion model and the associated blending coefficient, ω_d, a conditional-probability local analysis is performed over the results provided by three LRR simulations concerning Case 1, within the whole set of 5 simulations returned by Gauss-Legendre-based Smolyak sparse quadrature. Going into detail, the set of three simulations is characterized by three different values of ω_d, corresponding to the Gauss-Legendre quadrature points for the RV ξ_1, i.e., $\omega_d = \{0.112702, 0.5, 0.887299\}$, whereas Sc_t is set to 0.6. Then, the conditional-probability local analysis is carried out to calculate the probability distribution of the droplets' distance from the inflow section, δ_d, conditional on specific values taken by the acetone vapor mass fraction, Y_v, in the proximity of droplet surface. Specifically, the conditional PDF of δ_d, given the value $\overline{Y}$ taken by Y_v, may be expressed as:

$$f_{\delta_d|Y_v}(\overline{\delta} \mid \overline{Y}) = \frac{f_{\delta_d,Y_v}(\overline{\delta}, \overline{Y})}{f_{Y_v}(\overline{Y})}, \tag{26}$$

where $f_{\delta_d,Y_v}(\overline{\delta}, \overline{Y})$ denotes the joint density of δ_d and Y_v, whereas $f_{Y_v}(\overline{Y})$ indicates the marginal density of Y_v.

Here, it is decided to take into account two different values of Y_v, i.e., $Y_v = \{0.045, 0.09\}$, that correspond to 25 and 50% of $Y_{v,s}(T_0, p_0)$, respectively. Then, this set of values for Y_v allows for generating two conditional PDFs for each of the three RANS simulations being considered, which are reported in Figure 12. As may be easily deducted, the selection of the lowest value of the dispersion model blending coefficient, i.e., $\omega_d = 0.112702$, returns platykurtic conditional distributions, characterized by largely negative values of kurtosis. This derives from a dispersion model tending

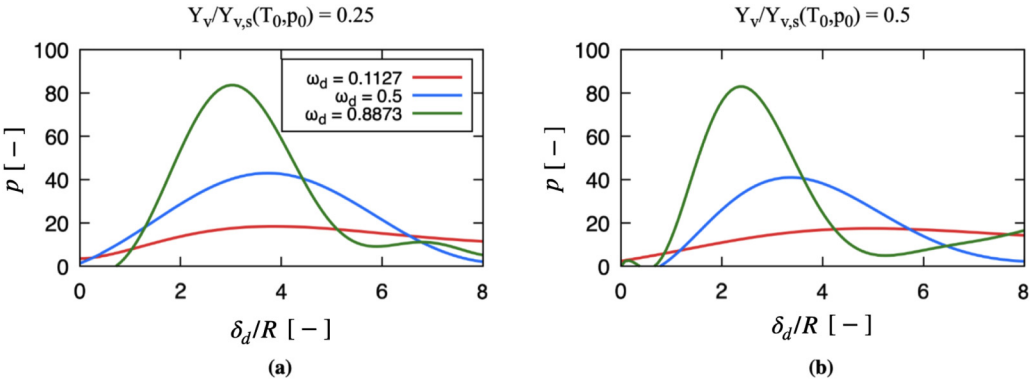

Figure 12. Case 1 (LRR model), conditional PDFs of droplets' distance from the inflow orifice, δ_d, given the surface vapor mass fraction, Y_v, for different values of the dispersion model blending coefficient, ω_d: (a) $Y_v/Y_{v,s}(T_0, p_0) = 0.25$, and (b) $Y_v/Y_{v,s}(T_0, p_0) = 0.5$.

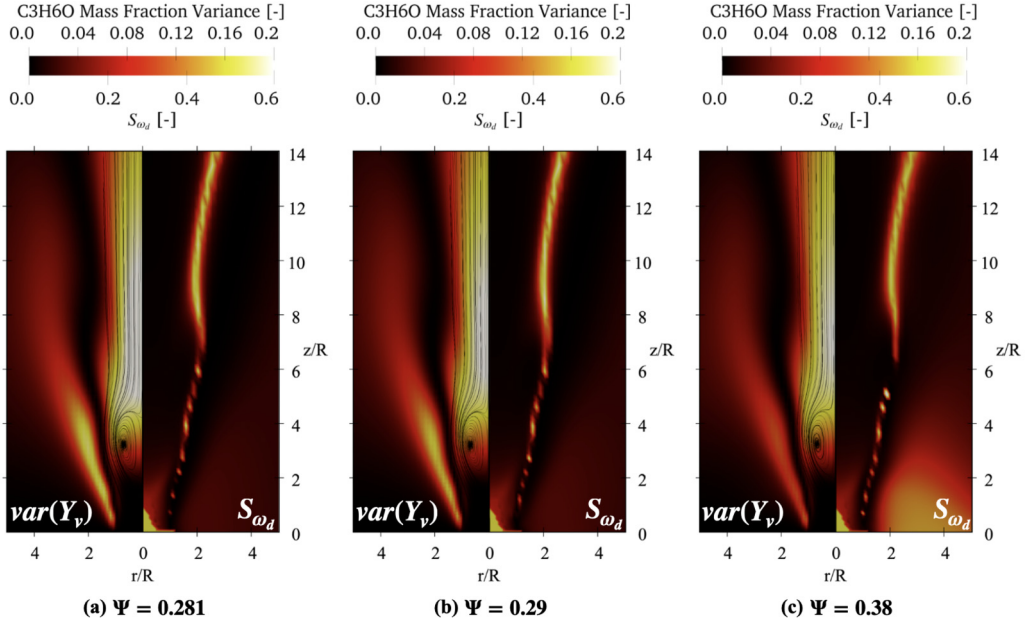

Figure 13. Case 1, variance-based sensitivity analysis of Y_v via LRR model for increasing liquid acetone mass flow rate: (a) $\Psi = 0.281$, (b) $\Psi = 0.29$, and (c) $\Psi = 0.38$.

towards a purely DRW-driven approach, which hinges on an intrinsically stochastic background. On the other hand, for increasing values of the blending coefficient, the resulting conditional PDFs show a more restricted range of droplets distance from the inflow section, given one specific value of Y_v at the droplet surface. In conclusion, this analysis clearly shows how the droplet dispersion model locally plays an active role in liquid droplets' spatial distribution. However, as previously highlighted, its influence over the acetone vapor mass fraction field is almost negligible compared to the effects of the turbulent Schmidt number.

Sensitivity to droplet dispersion model at increasing mass loading

Finally, the sensitivity of the output variance to the droplet dispersion model is further investigated by employing three additional forward UQ analyses concerning Case 1, with increasing liquid mass loading. In particular, the liquid acetone mass flow rate, $\dot{m}_{act,v}$, is selected to be 10, 100, and 1000 times higher than the nominal flow rate, respectively, thus affecting the overall aerodynamic response properties of the liquid phase. In contrast, the gaseous acetone mass flow rate, $\dot{m}_{act,v}$, and the air mass flow rate, $\dot{m}_{air}$, are kept fixed,

along with the size and the velocity of the liquid droplets. Specifically, the acetone-to-air mass flow rate ratio takes different values, i.e., $\Psi = \{0.281, 0.29, 0.38\}$.

In this regard, Figure 13 illustrates the field distribution of the first-order Sobol index for ω_d as concerns the different values of Ψ, accompanied with the variance of Y_v, as computed from equation (23). In the first place, it must be noted that the variance of Y_v remains mostly concentrated in the near-field mixing layer and the far-field vortex core, regardless of the liquid mass loading. Nevertheless, the overall output variance in the near-field velocity shear layer progressively diminishes for increasing values of Ψ, see Figure 13(c). Concerning the contribution of ω_d to the variance of Y_v, the droplet dispersion model keeps playing an active role predominantly in the far-field mixing layer, characterized by an overall vanishing output variance, for different values of the acetone-to-air mass flow rate ratio. Exclusively under extremely high liquid mass loading, i.e., $\Psi = 0.38$, the droplet dispersion model significantly contributes to the acetone vapor mass fraction's variance beyond the near-field mixing layer. In particular, as shown in Figure 13(c), the main-effect Sobol index for ω_d takes considerable values in the proximity of the vortex-expansion region, approximately from $r/R = 2$ to $r/R = 5$. However, such a region still exhibits an overall vanishing output variance. Therefore, given the nearly-saturated inflow condition, it can be concluded that the field distribution of acetone vapor mass fraction is slightly affected by the droplet dispersion model, regardless of the liquid acetone mass flow rate injected into the domain.

Conclusions

The present work exploits the Bayesian UQ framework and PCEs to quantify the effects of select model uncertainties on a prototypical acetone/air spray swirling jet, resembling the flow field experienced by swirl-stabilized combustors for aeronautical applications. The configuration is first investigated via DNS for low- and high-swirl operating conditions, resulting in the onset of a bubble-type and regular conical VB, respectively. Then, based on the available high-fidelity data, a preliminary analysis is conducted to assess the most suitable models for Reynolds stresses closure in the RANS approach, providing the NLEVM and LRR models for low-swirl conditions, and the kEps-RNG and LRR models for high-swirl conditions, as those closure models most in agreement with DNS results. The focus is consequently placed on the forward propagation of modeling uncertainty associated with the droplet dispersion model and the turbulent Schmidt number, performed via a non-intrusive spectral projection technique for each of the abovementioned closure models. The PCE representation of RVs enables the construction of surrogate models for the selected QoIs, namely, the velocity vector field and the acetone vapor mass fraction, that are exploited to visualize pushforward distributions and confidence intervals, here compared to reference DNS data. Furthermore, the sensitivity of output variance is investigated utilizing global Sobol sensitivity analysis, naturally embedded within the UQ framework. The following conclusions can be drawn from the present study:

- high-fidelity DNS data are crucial to perform an ad hoc selection of the most suitable Reynolds stresses RANS closure as concerns the vortex-breakdown-affected swirling configuration of interest, as discussed in the "Direct numerical simulation results" section;
- most of RANS closure models are inadequate to capture the kinematic features of both bubble-type and regular conical VB states, as discussed in the "Reynolds stresses closure in RANS" section;
- the LRR model is the most versatile approach for moderately to highly swirling flows and may be further improved by enhancing the modeling of turbulence dissipation tensor's anisotropic features, which is postponed to our future work, as discussed in the "Second-Moment closure models" section;
- the spray dispersion model barely affects the fundamental QoIs, as discussed in the "Main observables and error bars" section, regardless of the mass loading of the injected liquid phase (see the "Sensitivity to droplet dispersion model at increasing mass loading" section); still, it plays an active role on local spatial droplets distribution, as discussed in the "Liquid-Phase conditional-probability local analysis" section;
- the choice of the turbulent Schmidt number induces a significant variance in the field distribution of fuel vapor mass fraction, eventually causing an overlap of computational model outputs associated with different turbulence closure models, as discussed in the "Main observables and error bars" section;
- information from the global sensitivity analysis, presented in the "Main observables and error bars" section, proves vital in driving additional high-fidelity experimental and/or numerical campaigns devoted to reducing model uncertainty via ad hoc calibration procedures based on inverse UQ strategies; indeed, given the outcome of such analysis, the choice of the spray dispersion model may be regarded as a second-class uncertainty, whereas research effort should be placed on developing an improved formulation for the turbulent Schmidt number.

Based on this, the proposed strategy may be regarded as a potential instrument to enrich the preliminary stage of a computational-aided design of aerospace combustion devices, resulting in a reliable, robust design optimization process.

Declaration of conflicting interests

The author(s) declare no potential conflicts of interest with respect to the research, authorship, and/or publication of this article.

Funding

The author(s) received no financial support for this article's research, authorship, and/or publication.

ORCID iD

Jacopo Liberatori https://orcid.org/0000-0002-6394-5250

References

1. Kurzawska P. Overview of sustainable aviation fuels including emission of particulate matter and harmful gaseous exhaust gas compounds. *Transp Res Proc* 2021; 59: 38–45.
2. Quante G, Bullerdiek N, Bube S et al. Renewable fuel options for aviation – A system-wide comparison of drop-in and non drop-in fuel options. *Fuel* 2023; 333: 126269.
3. Palies PP. Challenges and outlook for hydrogen-based aviation. In: *AIAA AVIATION 2022 Forum*, Chicago, IL, USA - Virtual, 27 June - 1 July 2022, paper no. AIAA 2022-3378. Reston: AIAA.
4. Huete J, Nalianda D and Pilidis P. Propulsion system integration for a first-generation hydrogen civil airliner? *Aeronaut J* 2021; 125: 1654–1665.
5. Lee B and Karkkainen RL. Failure investigation of hydrogen induced cracking of stabilator skin in jet aircraft. *Eng Fail Anal* 2018; 92: 182–194.
6. Marrero-Santiago J, Collin-Bastiani F, Riber E et al. On the mechanisms of flame kernel extinction or survival during aeronautical ignition sequences: experimental and numerical analysis. *Comb Flame* 2020; 222: 70–84.
7. Palies PP. Hydrogen thermal-powered aircraft combustion and propulsion system. *J Eng Gas Turbines Power* 2022; 144: 101007.
8. Colozza AJ. Hydrogen Storage for Aircraft Applications Overview. NASA/CR-2002-211867, National Aeronautics and Space Administration, Glenn Research Center, USA, 2002.
9. Veynante D and Vervisch L. Turbulent combustion modeling. *Prog Energy Combust Sci* 2002; 28: 193–266.
10. Trisjono P and Pitsch H. Systematic analysis strategies for the development of combustion models from DNS: A review. *Flow Turbul Combust* 2015; 95: 231–259.
11. Giusti A and Mastorakos E. Turbulent combustion modelling and experiments: Recent trends and developments. *Flow Turbul Combust* 2019; 103: 847–869.
12. Elghobashi S. Particle-laden turbulent flows: direct simulation and closure models. *Appl Sci Res* 1991; 48: 301–314.
13. Chen X-Q and Pereira JC. Computation of turbulent evaporating sprays with well-specified measurements - A sensitivity study on droplet properties. *Int J Heat Mass Transf* 1996; 39: 441–454.
14. Balachandar S and Eaton JK. Turbulent dispersed multiphase flow. *Annu Rev Fluid Mech* 2010; 42: 111–133.
15. Jenny P, Roekaerts D and Beishuizen N. Modeling of turbulent dilute spray combustion. *Prog Energy Combust Sci* 2012; 38: 846–887.
16. Dalla Barba F and Picano F. Clustering and entrainment effects on the evaporation of dilute droplets in a turbulent jet. *Phys Rev Fluids* 2018; 3: 034304.
17. Ciottoli PP, Battista F, Malpica Galassi R et al. Direct numerical simulations of the evaporation of dilute sprays in turbulent swirling jets. *Flow Turbul Combust* 2021; 106: 993–1015.
18. Liberatori J, Battista F, Dalla Barba F et al. Direct numerical simulation of vortex breakdown in evaporating dilute sprays. *Flow Turbul Combust* 2023. submitted for publication.
19. MacKay DJC. *Information Theory, Inference, and Learning Algorithms*. 1st ed.Cambridge: Cambridge University Press, 2005.
20. Safta C, Sargsyan D, Najm HN et al. Uncertainty Quantification Methods for Model Calibration, Validation, and Risk Analysis. In: *16th AIAA Non-Deterministic Approaches Conference*, National Harbor, Maryland, USA, 13-17 January 2014, paper no. AIAA 2014-1497. Reston: AIAA.
21. Hakim L, Lacaze G, Khalil M et al. Probabilistic parameter estimation in a 2-step chemical kinetics model for n-dodecane jet autoignition. *Combust Theory Model* 2018; 22: 446–466.
22. Cortesi A, Constantine P, Magin T et al. Forward and backward uncertainty quantification with active subspaces: application to hypersonic flows around a cylinder. *J Comput Phys* 2020; 407: 109079.
23. Armengol JM, Le Maître O and Vicquelin R. Bayesian calibration of a methane-air global scheme and uncertainty propagation to flame-vortex interactions. *Combust Flame* 2021; 234: 111642.
24. Najm HN. Uncertainty quantification and polynomial chaos techniques in computational fluid dynamics. *Annu Rev Fluid Mech* 2009; 41: 35–52.
25. Malpica Galassi R, Valorani M, Najm HN et al. Chemical model reduction under uncertainty. *Combust Flame* 2017; 179: 242–252.
26. Ciottoli PP, Petrocchi A, Malpica Galassi R et al. Uncertainty quantification analysis of RANS of spray jets. In: *AIAA Propulsion and Energy 2020 Forum*, Virtual Event, 24-28 August 2020, paper no. AIAA 2020-3882. Reston: AIAA.
27. Liberatori J, Malpica Galassi R, Liuzzi D et al. Uncertainty quantification in RANS prediction of LOX cross-flow injection in Methane. In: *AIAA Propulsion and Energy 2021 Forum*, Virtual Event, 9-11 August 2021, paper no. AIAA 2021-3570. Reston: AIAA.
28. Cavalieri D, Liberatori J, Malpica Galassi R et al. Unsteady RANS Simulations with Uncertainty Quantification of Spray Combustor Under Liquid Rocket Engine Relevant Conditions. In: *AIAA SciTech 2023 Forum*, National Harbor, MD & Online, 23-27 January 2023, paper no. AIAA 2023-2148. Reston: AIAA.
29. Battista F, Troiani G and Picano F. Fractal scaling of turbulent premixed flame fronts: Aaplication to LES. *Int J Heat Fluid Flow* 2015; 51: 78–87.
30. Ciottoli PP, Lee BJ, Lapenna PE et al. Large eddy simulation on the effects of pressure on syngas/Air turbulent nonpremixed jet flames. *Combust Sci Technol* 2020; 192: 1963–1996.
31. Huang Y and Yang V. Effect of swirl on combustion dynamics in a lean-premixed swirl-stabilized combustor. *Proc Combust Inst* 2005; 30: 1775–1782.
32. Huang Y and Yang V. Dynamics and stability of lean-premixed swirl-stabilized combustion. *Prog Energy Combust Sci* 2009; 35: 293–364.
33. Samarasinghe J, Peluso SJ, Quay BD et al. The three-dimensional structure of swirl-stabilized flames in a lean

premixed multinozzle can combustor. *J Eng Gas Turbines Power* 2016; 138: 031502.
34. Billant P, Chomaz JM and Huerre P. Experimental study of vortex breakdown in swirling jets. *J Fluid Mech* 1998; 376: 183–219.
35. Lucca-Negro O and O'Doherty T. Vortex breakdown: a review. *Prog Energy Combust Sci* 2001; 27: 431–481.
36. Escudier M. Vortex breakdown: observations and explanations. *Prog Aerosp Sci* 1988; 25: 189–229.
37. Brucker C and Althaus W. Study of vortex breakdown by particle tracking velocimetry part 1: Bubble-type vortex breakdown. *Exp Fluids* 1992; 13: 339–349.
38. Garg AK and Leibovich S. Spectral characteristics of vortex breakdown flowfields. *Phys Fluids* 1979; 22: 2053–2064.
39. Gokulakrishnan P, Ramotowski MJ, Gaines G et al. A novel low NOx lean, premixed, and prevaporized combustion system for liquid fuels. *J Eng Gas Turbines Power* 2008; 130: 051501.
40. Eskin LD, Holton MM, Turner BA et al. Long-Term Demonstration of a Lean, Premixed, Prevaporized (LPP) System for Gas Turbines. In: *20th International Conference on Nuclear Engineering*, Anaheim, California, USA, 30 July - 3 August 2012, paper no. ICONE20-POWER2012-54766, pp. 737-745. New York: ASME.
41. Keller JJ. Thermoacoustic oscillations in combustion chambers of gas turbines. *AIAA J* 1995; 33: 2280–2287.
42. Lieuwen T and McManus K. Combustion dynamics in lean-premixed pre-vaporized gas turbine. *J Propuls Power* 2003; 19: 721.
43. Mueller M and Raman V. Model form uncertainty quantification in turbulent combustion simulations: Peer models. *Comb Flame* 2018; 187: 137–146.
44. Ruith MR, Chen P and Meiburg E. Development of boundary conditions for direct numerical simulations of three-dimensional vortex breakdown phenomena in semi-infinite domains. *Comput Fluids* 2004; 33: 1225–1250.
45. Sheen HJ, Chen WJ, Jeng SY et al. Correlation of swirl number for a radial-type swirl generator. *Exp Therm Fluid Sci* 1996; 12: 444–451.
46. Choi J and Do H. Modeling swirl decay rate of turbulent flows in annular swirl injectors. *AIAA J* 2018; 56: 4910–4926.
47. Jalalatian N, Tabejamaat S, Kashir B et al. An experimental study on the effect of swirl number on pollutant formation in propane bluff-body stabilized swirl diffusion flames. *Phys Fluids* 2019; 31: 055105.
48. Hadziabdic M, Halilagic M and Hanjalic K. RANS investigation of hysteresis of vortex breakdown in the cold model of a swirl burner. In: *7th International Symposium on Turbulence, Heat and Mass Transfer*, Palermo, Sicily, Italy, 24 - 27 September 2012, pp. 1021–1039.
49. Foroutan H and Yavuzkurt S. A partially-averaged navier–stokes model for the simulation of turbulent swirling flow with vortex breakdown. *Int J Heat Fluid Flow* 2014; 50: 402–416.
50. Spalart P and Allmaras S. A one-equation turbulence model for aerodynamic flows. Technical Report AIAA-92-0439, American Institute of Aeronautics and Astronautics, USA, 1992.
51. Dacles-Mariani J, Zilliac GG, Chow JS et al. Numerical/Experimental study of a wingtip vortex in the near field. *AIAA J* 1995; 33: 1561–1568.
52. Launder BE and Spalding DB. The numerical computation of turbulent flows. *Comput Methods Appl Mech Eng* 1974; 3: 269–289.
53. Shih TH, Liou WW, Shabbir A et al. A new k-ϵ eddy viscosity model for high Reynolds number turbulent flows. *Comput Fluids* 1995; 24: 227–238.
54. Yakhot V, Orszag SA, Thangam S et al. Development of turbulence models for shear flows by a double expansion technique. *Phys Fluids A: Fluid Dynamics* 1992; 4: 1510.
55. Erhard J and Moussiopoulos S. On a new nonlinear turbulence model for simulating flows around building-shaped structures. *J Wind Eng Ind* 2000; 88: 91–99.
56. Pope SB. *Turbulent Flows*. 1st ed. Cambridge: Cambridge University Press, 2000.
57. Launder BE, Reece GJ and Rodi W. Progress in the development of a reynolds-stress turbulence closure. *J Fluid Mech* 1975; 68: 537–566.
58. Rotta J. Statistische theorie nichthomogener turbulenz. *Zeitschrift für Physik* 1951; 129: 547–572.
59. Speziale CG, Sarkar S and Gatski TB. Modelling the pressure-strain correlation of turbulence. An invariant dynamical systems approach. *J Fluid Mech* 1991; 227: 245–272.
60. Speziale CG and Gatski TB. Analysis and modelling of anisotropies in the dissipation rate of turbulence. *J Fluid Mech* 1997; 344: 155–180.
61. Yang X, Gui N, Xie G et al. Anisotropic characteristics of turbulence dissipation in swirling flow: A direct numerical simulation study. *Adv Math Phys* 2015; 2015: 657620.
62. Jiang L-Y and Campbell I. Prandtl/Schmidt number effect on temperature distribution in a generic combustor. *Int J Therm Sci* 2009; 48: 322–330.
63. Gosman AD and Ioannides E. Aspects of computer simulation of liquid-fueled combustors. *J Energy* 1983; 7: 482–490.
64. Ivanova EM, Noll BE and Aigner M. A numerical study on the turbulent Schmidt numbers in a jet in crossflow. *J Eng Gas Turbines Power* 2013; 135: 011505.
65. Donzis DA, Aditya K, Sreenivasan KR et al. The turbulent Schmidt number. *J Fluids Eng* 2014; 136: 061210.
66. Xiao X, Hassan HA and Baurle RA. Modeling Scramjet flows with variable turbulent Prandtl and Schmidt numbers. *AIAA J* 2007; 45: 1415–1423.
67. Keistler PG, Hassan HA and Xiao X. Simulation of supersonic combustion in three-dimensional configurations. *J Propuls Power* 2009; 25: 1233–1239.
68. Goldberg UC, Palaniswamy S, Batten P et al. Variable turbulent schmidt and prandtl number modeling. *Eng Appl Comput Fluid Mech* 2010; 4: 511–520.
69. Longo R, Bellemans A, Derudi M et al. A multi-fidelity framework for the estimation of the turbulent schmidt number in the simulation of atmospheric dispersion. *Build Environ* 2020; 185: 107066.
70. McClarren RG. *Uncertainty Quantification and Predictive Computational Science, A Foundation for Physical Scientists and Engineers*. 1st ed. Cham: Springer, 2018.